RSC Advances




ROYAL SOCIETY OF CHEMISTRY

www.rsc.org/advances

# Enhancement of Magnetic Heating Efficiency in Size Controlled $MFe_2O_4$ (M = Mn, Fe, Co and Ni) Nanoassemblies

Jeotikanta Mohapatra,[a] Saumya Nigam,[b] J. Gupta,[c] A. Mitra,[d] M. Aslam,[a,d,*] D. Bahadur,[a,c,*]

[a]Centre for Research in Nanotechnology and Science (CRNTS), [b]IITB-Monash Research Academy, [c]Department of Metallurgical Engineering and Materials Science, [d]Department of Physics, Indian Institute of Technology Bombay, Powai, Mumbai-40076, India

**To whom correspondence should be addressed.* m.aslam@iitb.ac.in. (M. Aslam). *Phone: +91 22 2576 7585, E-mail:* dhirenb@iitb.ac.in. (D. Bahadur), *Phone: +91 22 2576 7632*

**Abstract:**

The $MFe_2O_4$ magnetic nanoparticle nanoassemblies (MNNAs) have been synthesized via thermal decomposition of metal chloride in ethylene glycol (EG) in the presence of ethylenediamine (EDA). The size of the nanoassemblies is controlled in the range of 25-60 nm by manipulation of Fe-precursor mole content to ethylene glycol (EG) and from 60 to 135 nm by using a bi-solvent mixture of ethylene glycol and polyethylene glycol (PEG-400). In this study, we demonstrate optimization of magnetic fluid heat activation by tailoring the size of $MFe_2O_4$ (M = Mn, Fe, Co and Ni) MNNAs. The densely packed nanocrystals within the MNNAs induce strong exchange as well as dipolar interactions between the nanocrystals, which increases the total magnetic moment for MNNAs. Additionally the magnetization ($M_S$, magnetization in a field of 20 kOe) of MNNAs decreases in an order as Mn> Fe > Co> Ni due to cationic distribution of ions with varying magnetic moments in these spinel oxides. A sharp increase of heating efficiency for 25-60 nm assembled particles could be attributed to the collective Néel relaxation of nanocrystals within the assemblies and also due to high particle magnetic moment, which increases with the MNNAs size. Furthermore, among all the $MFe_2O_4$ nanoassemblies of various sizes, $Fe_3O_4$ MNNAs with an average diameter of 80 nm show an excellent SAR value of 646

W/g of $Fe_3O_4$ at 247 kHz with an applied AC magnetic field of 310 Oe, which is 2-4 times higher than that of the single domain assembled nanoparticles. The moderate anisotropy constant and high $M_S$ values of $Fe_3O_4$ MNNAs make it most suitable candidate to produce the highest heating power. These magnetic MNNAs are efficient in killing the cancer cells by the application of AC magnetic field even for a short treatment time of 30 min.

**Keywords**: Spinel oxide, Nanocrystals nanoassembly, Superparamagnetic, Magnetic heating

## 1. Introduction

Spinel metal-oxide nanoparticles of generic formulation $MFe_2O_4$ (M = Mn, Fe, Co or Ni) have been studied extensively in recent years for their promising biomedical applications, such as contrast agents in magnetic resonance imaging (MRI), vectors in drug delivery and mediators to convert electromagnetic energy to heat, when subjected to an alternating current magnetic field (ACMF).[1-5] The latter 'heat activation by magnetic fluid' is an emerging technology which is currently being explored for hyperthermia cancer treatment, thermally activated drug release, remote activation of cell functions, etc.[6-9] However, for most of these exciting new therapeutic applications, relatively poor heating ability of the nanoparticles presents a challenging obstacle, which either needs a strong magnetic field or requires relatively large amounts of nanoparticles, resulting in the harmful side-effects.[10] For this purpose, a high efficiency magnetic heating agent is necessitated, which can be achieved by designing a new class of functional nanomaterials with high saturation magnetization ($M_S$) and moderate effective anisotropy constant ($K_{eff}$).[11] To date, many challenges have been taken to optimize the magnetic properties of iron oxide nanostructures for the enhancement of the heating ability.[12, 13] For example, nanoparticles with hard and soft ferrite core-shell architecture were observed to exhibit enhanced magnetic heating power due to high exchange coupling.[14] A strong exchange coupling

optimizes the $K_{eff}$ to an intermediate value of soft and hard ferrite and makes the nanoparticles relax with a frequency of applied ac magnetic field. Recently, the multi-domain magnetic nanostructures such as nanoflowers and nanocrystals assemblies have also shown efficient heating power due to cooperative magnetism among nanocrystals within the multi-domain nanostructure.[15-17] However, the dependence of heating efficiency on the structural and magnetic characteristics needs to be explored further.

Herein, a simple approach for the synthesis of aqueous stable amine functionalized monodisperse MNNAs of size 25-135 nm is developed. The as-synthesized nanoassemblies have cubic spinel structure as characterized by electron microscopy and X-ray diffraction (XRD) studies. All the samples show a superparamagnetic behavior at room temperature and have high $M_S$ values due to synergistic interactive magnetism imminent from multiple nanocrystals assembled in MNNAs. Among all the $MFe_2O_4$ nanoassemblies of different sizes, $Fe_3O_4$ MNNAs with an average diameter of 80 nm show an excellent SAR value of 646 W/g of $Fe_3O_4$, which is 2-4 times higher than that of the single domain assembled nanoparticles.

## 2. Experimental Method

### Synthesis of $MFe_2O_4$ (M = Mn, Fe, Co or Ni) MNNAs

$MFe_2O_4$ (M = Mn, Fe, Co or Ni) magnetic nanocrystal nanoassemblies were prepared by a modified thermal decomposition approach.[18] In a typical synthesis of 50 nm MNNAs, 4 mmol of $FeCl_3$, 2 mmol of $MCl_2$ and 8 ml of ethylenediamine in ethylene glycol (30 ml) was stirred vigorously by a magnetic stirrer at 50 °C to obtain a clear homogeneous golden yellow colored solution. The solution was then transferred into a teflon-lined stainless steel autoclave of 50 ml capacity. Before sealing the autoclave, argon was bubbled into the solution to remove the air. The autoclave was initially maintained at 120 °C for 30 min and then quickly heated to 180 °C at

a heating rate of 10 °C/min and aged for 2 h. After completion of the reaction, the autoclave was cooled to room temperature. The magnetic particles were separated from the solvent by using a permanent magnet and thoroughly rinsed with ethanol. The size of nanoassemblies (keeping the nanocrystallite size approximately same) was controlled from 25 to 60 nm by controlling the mole content of metal chloride-precursor ($Fe^{3+}/M^{2+}$ = 2:1), while the size above 60 nm were prepared by taking a bi-solvent mixture of EG and polyethylene glycol (PEG-400) (a stronger reducing agent). The effect of PEG amount on size of $Fe_3O_4$ MNNAs is summarized in Table 1. The increase in the PEG content from 2 to 12 ml results in an increase of nanoassemblies' size (60-135 nm) as well as nanocrystals' size (8 to 22 nm). Scheme 1 depicts the details of the synthesis approach undertaken.

**Surface Stabilization by Polyethyleneimine**

To increase the colloidal stability, the as prepared $MFe_2O_4$ MNNAs were subjected to surface modification with polyethyleneimine (PEI). 100 mg of the as prepared $MFe_2O_4$ nanoparticles were dispersed in 30 mL of ethanol and after complete dispersion, 0.5 g PEI solution with 10 ml deionized water was added to this mixture. Under $N_2$ ambience, the mixture was then continuously stirred at 100 °C for 8 h. After the reaction, the final product was subjected to magnetic separation and was washed with ethanol several times to remove uncoordinated PEI molecules. The resultant particles were easily dispersed in deionized water and chosen for material characterizations and magnetic heating studies.

***In vitro* magnetic heat activation studies**

There are two methods of administering magnetic hyperthermia, external and internal. For undertaking external hyperthermia, the magnetic nanoparticles' suspension along with the cell suspension is first exposed to ACMF for desired duration and then incubated for some time.

The internal hyperthermia, on the other hand involves first incubating the nanoparticles with cells to facilitate their internalization and then subsequent exposure to ACMF. We have followed the former for our studies. The human cervical cancer (HeLa) cells were grown in minimum essential medium (MEM) supplemented with fetal bovine serum (FBS) and penicillin/streptomycin antibiotics at 37 °C in a 5% $CO_2$ environment. After the culture reached 90% confluency, the cells were trypisinized, collected by centrifugation and re-suspended in 500µl of supplemented MEM. 100µl of this cell suspension was then added to 100µl of trypan blue. The cells were counted to a cell density of $1\times10^6$ cells by the trypan blue exclusion method.[19] 250µl (2 mg/ml) of sterile MNNA suspension (sterility by exposure to UV light) was added to the cell suspension and the volume was made up to 1 ml by the supplemented MEM. It was then exposed to an ACMF (fixed frequency; 247 kHz) of 310 Oe for initial 10 min to reach the hyperthermia temperature of 45±1 °C and later maintained at 45±1°C by lowering the applied field to 259 Oe for different treatment time intervals (15, 20, 25 and 30 min). The cell suspension was then seeded in a 30 mm petridish with an additional 1 ml of supplemented MEM and incubated for 6, 12 and 24 h at 37 °C in a 5 % $CO_2$ environment (The results after 6 hours showed optimal fatal effects on cancer cells after minimum incubation time and thus was reported to present the efficacy of these MNNAs within limited time). The cells were then trypsinized and counted for viable cell population by the trypan blue exclusion method. The viable cell population was represented as under:

$$\%\ Viable\ cells\ = \frac{No.\ of\ live\ cells}{Total\ cells\ incubated}\times 100 \quad \ldots\ldots\ldots\ldots\ldots\ldots\ldots\ldots\ (1)$$

**3. Results and discussion**

The X-ray diffraction patterns of $MFe_2O_4$ MNNAs of size 80 nm (Fig. 1a) reveals cubic spinel structure, exhibiting six prominent peaks, which originate from the (220), (311), (400), (422), (511) and (440) planes. The crystallite size determined by Scherrer equation [20] from (311) peak is around 14 nm, which suggests that the prepared 80 nm $MFe_2O_4$ MNNAs are composed of nanocrystals with a diameter of 14 nm. The porous morphology of $Fe_3O_4$ MNNAs is confirmed by measuring the adsorption and desorption isotherms of $N_2$ (Fig. 1b). The Brunauer-Emmett-Teller (BET) surface area of 80 nm $Fe_3O_4$ MNNAs is calculated as 104 ± 1.2 $m^2/g$. The pore size distribution of the sample demonstrates two distinct peaks, one at 4 nm corresponds to the pore diameter of the nanoassembly and the other peak at 30 nm could be attributed to the interspace among the nanoassembly.

The surface coating of PEI is confirmed from the Fourier transform infrared (FTIR) spectroscopy and ζ-potential measurements. The FTIR spectra of both as prepared and PEI functionalized $Fe_3O_4$ MNNAs (80 nm) (Fig. S1, ESI) shows peaks at 3740 $cm^{-1}$ (N-H stretching mode of primary amine) and 1068 $cm^{-1}$ (C-N stretching). In comparison to as prepared $Fe_3O_4$ MNNAs, PEI functionalized $Fe_3O_4$ samples show strong IR peaks corresponding to C−N stretching, $NH_2$ scissoring and N-H stretching which confirm the presence of PEI on the surface of $Fe_3O_4$ MNNAs. Moreover, the low frequency band at around 578 $cm^{-1}$ refers to Fe-O vibration ($Fe^{3+}$ bond) in octahedral and tetrahedral sites, which could be attributed to the spinel ferrite phase of $Fe_3O_4$ while the Fe-O band for γ- $Fe_2O_3$ is usually seen at 540 $cm^{-1}$.[21] Fig. 1c shows thermogravimetric (TGA) degradation profiles of the as-prepared and PEI-coated $Fe_3O_4$ MNNAs. A prominent weight loss over the temperature range of 150-450 °C is observed which could be attributed to the decomposition of the PEI and PEG molecules attached to the particle surface. The large weight loss in PEI-coated MNNAs confirms the coating of PEI on

nanoassemblies surface. We believe that very slow and delayed oxidation of $Fe^{2+}$ around 450 °C is due to protective nature of capping molecules on the nanoparticles' surface, which has been reported earlier for magnetite structures.[22] Further, ζ-potential measurements of the as-prepared MNNAs and PEI coated MNNAs were performed under the influence of varying pH (Fig. 1d). The isoelectric point of as-prepared MNNAs lies between pH 4 and 5 while a shift in the isoelectric points of PEI coated MNNAs to higher values is observed. The aqueous suspension of as-prepared MNNAs is seen to be negatively charged while the PEI coated MNNAs show a charge reversal in the pH range of 5 to 9. The higher ζ-potential values (≥ 30 mV) in the pH range of 3 to 8 affirm the aqueous stability of the PEI coated MNNAs.

Fig. 2 shows the representative TEM images of the $Fe_3O_4$ MNNAs synthesized with different amount of Fe-precursor with EG as solvent. A statistical analysis has been done for each sample by counting almost 45-60 particles. The average MNNAs size is estimated from TEM micrograph using the lognormal distribution (see inset Fig. 2). All of the synthesized magnetic particles have nearly spherical shape and uniform size ($\sigma \leq 20$ %). With an increase in the Fe-precursor ($Fe^{3+}/Fe^{2+}$ = 2:1) content to 1.5, 3, 4.5, 6 and 7.5 mmol; the average diameter of the obtained particles are 25, 30, 40, 50 and 60 nm, respectively. A further increase of Fe-precursor to 9 mmol does not give any control over shape, size and the phase (Fig. S2, ESI). The formation process of the ferrite MNNAs follows the reported two-stage growth model.[23] In the initial reaction step, M-ions are reduced by EG and DEA towards nucleation of $MFe_2O_4$ primary nanoparticles. The primary $MFe_2O_4$ nanoparticles then gradually aggregated to minimize the surface energy and result in the nanoassembled structures. However, the surface of the nanoparticles is capped by the PEG-amine, which is formed during the synthesis of nanoparticles via the polymerization of EG.[24] From TEM image (Fig. 2), the nanocrystallite size of these

MNNAs (25-60 nm) is found to be fairly uniformly distributed (d = 4 ± 1 nm) which corroborates with the values obtained from the XRD pattern (Fig. S3, ESI). Fig. 2f shows the selected area diffraction (SAED) pattern of $Fe_3O_4$ MNNAs of size 60 nm. The SAED pattern indicates a set of rings instead of spots due to the random orientation of the crystallites, corresponding to reflection from six crystal planes, indicating (220), (311), (400), (422), (511) and (440). This also supports the formation of spinel cubic phase of the MNNAs.

To increase the nanoassembly size (≥60 nm) as well as the nanocrystallite size (8-22 nm) further, PEG-400 which has stronger reducing ability than EG was used as an additional solvent. Fig. 3 shows the TEM images of the $Fe_3O_4$ MNNAs produced with different PEG content. The effect of the amount of PEG on the size of nanoassemblies is depicted in Table 1. The average diameter of the nanoassemblies radically increases from 60 to 135 nm with an increase of PEG content from 2 to 12 ml (Fig. S4, ESI), which indicates that the $Fe_3O_4$ nanoparticles have strong affinity towards the PEG chains and that can assemble to form large secondary structural $Fe_3O_4$ MNNAs. The increase in the PEG content from 2 to 12 ml is also seen to result in an increase in the average nanocrystallite size from 8 to 22 nm (inset of Fig. 3) and it also in agreement with the nanocrystallite values, obtained from the XRD spectra (Fig. S5, ESI). With further increase of PEG content to 16 ml and 20 ml, the morphology of the nanoparticle assemblies is transformed to a compact structure with a decrease of overall particle size to 120 and 80 nm, respectively (Fig. 3e and f). This decrease is attributed to the higher reducing and capping ability of PEG, which accelerates the generation of ferrous ions and promotes the formation of compact iron oxide nanoparticles.[25] This is also confirmed from the decrease in FWHM of the XRD peaks and the absence of porous morphology (surface area =72 ± 1 $m^2/g$) (Fig. S6, ESI) in sample produced with higher PEG (20 ml) content. The control exercised over both Fe-precursor mole

content and PEG to EG ratio enable to control the size of the nanoassemblies with higher precision as 25, 30, 40, 50, 60, 80, 110 and 135 nm (standard deviation $\sigma \leq 20$ %). Similar to $Fe_3O_4$ MNNAs, the size of $MFe_2O_4$ (M = Mn, Co and Ni) MNNAs are controlled from 25 -135 nm by controlling both metal chloride precursor mole content and PEG to EG volume. Fig. 4a-c shows the TEM image of $MFe_2O_4$ MNNAs (110 nm) prepared by using 8 ml PEG. Similar to $Fe_3O_4$ MNNAs, all of the synthesized ferrites MNNAs are uniform in shape and size ($\sigma \leq 20$ %). The elemental analysis using energy-dispersive X-ray spectroscopy (Fig. 4d-f) and inductively coupled plasma atomic emission spectroscopy (ICP-AES) (Table S1, ESI), demonstrates that both Fe and M (Mn, Co and Ni) elements are present (with a stoichiometry of 2:1) in the respective ferrite samples.

Fig. 5a-d shows the SEM images of the representative $Fe_3O_4$ MNNAs prepared by varying PEG content as 2, 5, 16 and 20 ml. The $Fe_3O_4$ MNNAs produced with low content of PEG leads to the formation of nanoassemblies, while with high PEG content (16 and 20 ml) the morphology of the nanoassembly is transformed to compact nanoparticles of size 120 and 80 nm, respectively. These results are in congruence with the TEM results to establish the higher content of PEG (above12 ml) favors the formation of nanoparticles rather than nanoassemblies.

On the basis of above experiments and analysis, we propose a probable mechanism of size controlled synthesis of MNNAs by using bi-solvent mixture of EG and PEG. In general, if the nanocrystals combine each other with the same crystal orientation, the MNNAs will be more stable in solution with minimum total surface energy.[26] As previously reported, in case of EG due to its mild reducing agent properties, the formation and growth rate of nanocrystals are slower than PEG.[16, 17] Hence each nanocrystal has enough time to rotate during ripening phase at high temperature to attach with the same crystal orientation and this leads to the formation of

MNNAs. On the contrary, due to strong reducing ability of PEG, the aggregation and growth of nanocrystals take place simultaneously and there is not enough time for the newly formed nanocrystals to rotate and attach with the neighboring nanocrystals along the same crystal orientation. This misalignment of nanocrystals' orientation enhances the interface energy in the MNNAs which collapses the three dimensional nanocrystals' assembly structure allowing the nanocrystals' to escape from the MNNAs. In our case, by using a bi-solvent mixture of EG and PEG, we have a control over the aggregation and growth of the nanocrystals. The increase in the PEG content from 2 to12 ml enables better control on the size of the MNNAs with higher precision as 60, 80, 110 and 135 nm. This size control is believed to be due to increased growth rate of nanocrystals, which increases with increase in PEG content. Further, the PEG content above 12 ml is seen to result in the formation of larger sized nanoparticles (120 and 80 nm) instead of the MNNAs, due to faster growth rate of nanocrystals.

Fig. 6a represents the zero field cool (ZFC) and field cool (FC) magnetization $M$(T) plots for different sized $Fe_3O_4$ (25- 60 nm) MNNAs prepared using EG as a solvent. A broad peak is observed in the $M_{ZFC}$ curve for all the samples at the blocking temperature ($T_B$), which shifts gradually towards higher temperature with an increase of MNNAs size. In general, for a system of magnetic particles with finite volume, $T_B$ varies linearly with the volume $V$ ($T_B = K_{eff}V/25k_B$).[27] But in our case, the nanocrystallite size of $Fe_3O_4$ MNNAs (25- 60 nm) is maintained the same. Thus we believe the linear increment of $T_B$ with the nanoassembly size could be due to magnetic couplings between the nanocrystals within the MNNA as the particle size in both the assemblies is same. Since the nanocrystals in the MNNA are in direct physical contact, exchange as well as dipolar couplings between them could be significant and contribute to enhance $T_B$. Thus, the increase of the nanoassembly size is seen to increase the magnetic coupling strength and thus

result in the enhancement of the blocking temperature. Another interesting feature of $M$ (T) curve is that $M_{FC}$ flattens out below $T_B$. In non-interacting magnetic nanoparticles (*viz.* superparamagnetic), the $M_{FC}$ continuously increases as the temperature is decreased. Whereas, our results show that the $M_{FC}$ remains flat below $T_B$ suggesting the presence of collective magnetic state due to magnetic interactions among the nanocrystals within the MNNA. This collective magnetic properties have been observed in self-assembled and cluster like nanoscale systems.[28, 29] Fig. 6b indicates the variation of $T_B$ with different size of $MFe_2O_4$ MNNAs. For all the samples, $T_B$ increases with increase in the size of nanoassembly. Among similar size of $MFe_2O_4$ MNNAs, $CoFe_2O_4$ exhibits extremely higher $T_B$ than others. For example, the $T_B$ for 60 nm $MnFe_2O_4$ MNNAs is 125 K, which is lesser by 75 K than that of the same size $CoFe_2O_4$ MNNAs. This deviation in $T_B$ for the same size of MNNAs with various $M^{2+}$ substituted spinel nanostructures is due to different magneto-crystalline anisotropy arising from the spin-orbit coupling strength of $M^{2+}$cations. The stronger spin-orbit coupling of $Co^{2+}$ ions leads to a larger $T_B$ for $CoFe_2O_4$ MNNAs.[30]

Fig. 6c shows the room temperature field dependent magnetization curve for different size of $Fe_3O_4$ (25-60 nm) MNNAs prepared by using EG only. All the samples show superparamagnetic properties with zero coercivity as well as remanence magnetization. The saturation magnetization $M_S$ (magnetization at field 20 kOe) shows an increasing trend with the increase of size of MNNAs. For example, the $M_S$ value for 25 nm $Fe_3O_4$ MNNAs is 48 emu/g and it increases to 75 emu/g for 60 nm $Fe_3O_4$ MNNAs. In addition to this, the observed $M_S$ values for different sizes are found to be higher as compared to that of the reported single nanocrystals counterparts.[31, 32] The magnetic exchange couplings between nanocrystals within the nanoassembly lead to decrease of the anisotropy energy, which allows increase of the total

magnetic moment for MNNA, $m_{total} = \sum_{\substack{i,j \\ i \neq j}} m_i + m_j + \Delta m_i m_j$ .[33] A similar increasing trend of $M_S$ values with MNNAs size is also observed for all the $MFe_2O_4$ MNNAs (Fig. 6d). The $M_S$ values of $MFe_2O_4$ MNNAs strongly depends on the magnitude of the $M^{2+}$ cation magnetic moment ($n\mu_B$, where $n$ = 5, 4, 3 and 2 for Mn, Fe, Co, and Ni, respectively).[34] The $M_S$ value of 60 nm $MnFe_2O_4$ MNNAs is 80 emu/g, which reduces as per the periodic arrangement to 75, 67 and 54 emu/g for $FeFe_2O_4$, $CoFe_2O_4$ and $NiFe_2O_4$ MNNAs, respectively. Such a control over the $M_S$ value with respect to magnetic coupling and composition is highly desirable for potential biomedical applications.

Fig. 7a represent the zero field cool (ZFC) and field cool (FC) magnetization $M$(T) plots for different sized $Fe_3O_4$ (60-135 nm) MNNAs prepared using PEG as well as EG. The $M_{ZFC}$ curve for all the samples shows a wider distribution of $T_B$ and could be attributed to its dependence on size distribution of nanocrystals as well as strong dipolar coupling. Further, in contrast to smaller size MNNAs (25-60 nm) the flatness of $M_{FC}$ curve is more prominent in $Fe_3O_4$ (60- 135 nm) MNNAs which is due to larger nanocrystals size. The larger nanocrystals display high magnetic moment and hence strong magnetic coupling, which extends the flatness of $M_{FC}$ curve to higher temperature. Fig. 7b shows the room temperature field dependent magnetization curve for different size $Fe_3O_4$ (60-135 nm) MNNAs. All the samples show superparamagnetic properties with zero coercivity and remanence. The $M_S$ values for all $MFe_2O_4$ MNNAs slowly increase with nanoassembly size (Fig. 7c). The $Fe_3O_4$ nanoparticles produced at higher content (≥ 16 ml) of PEG shows ferrimagnetic behavior with coercivity of 250 and 350 Oe for 80 and 120 nm particles, respectively (Inset; Fig. 7d).

The heating performance of the $MFe_2O_4$ MNNAs as a function of nanoassemblies and nanocrystals size was measured using a radio frequency generator operating at an applied ACMF of 310 Oe at a fixed frequency of 247 kHz. The initial temperature of the aqueous suspension of magnetic particles was set to a room temperature of 27 °C and then MNNA colloidal suspension is exposed to an ACMF for 900 s. Fig. 8a represents the comparative time dependent temperature profiles of $Fe_3O_4$ MNNAs (various sized 25-60 nm) having similar nanocrystallite size. The heating profile shows a sharp increase of temperature up to 300 s which then slows down and attains a plateau with time. This could be explained by the cooperative Néel relaxation of nanocrystals within the nanoassembly structure.[17, 18] The detailed analysis of SAR results as a function of both composition and size of $MFe_2O_4$ MNNAs are represented in Fig. 8b. Size dependent SAR value for $NiFe_2O_4$ MNNAs was not measured due to its low $M_S$ value. The SAR values of all the samples show an increase with an increase in size of MNNAs. This increase in SAR values indicates that the magnetic coupling may play an important role in defining the heating mechanisms. Both the theoretical and experimental investigations have shown that densely packed three dimensional nanoassemblies experience strong dipolar as well as exchange coupling between the nanoparticles.[17] Furthermore, the strong exchange coupling leads to decrease in the anisotropy energy, thereby increasing the total magnetic moment. Thus, under the influence of ACMF, a relatively more coherent magnetization direction reversal as well as shorter spin relaxation takes place. In our case, the nanocrystals within the MNNAs are in close contact and hence magnetic ordering and exchange coupling at the nanocrystals' interfaces is expected. Further, the findings from the magnetic characterization confirm the enhancement of $M_S$ value with the increase of MNNAs and the presence of a collective magnetic dynamics, i.e. collective magnetic behavior. So, we believe that the increase of heating efficiency with MNNAs

size is attributed to the collective Néel relaxation of nanocrystals within the assembly and also due to high particle magnetic moment, which increases with the MNNAs size. Another important finding is that in contrast to $CoFe_2O_4$ (high $K_{eff}$ value) and $MnFe_2O_4$ (high $M_S$), the $Fe_3O_4$ MNNAs have an exclusive highest SAR value in all the size range. Such a deviation in heating performance for various transition metals ($M^{2+}$) substituted spinel nanostructures can be explained by considering the theory of magnetic fluid heating, which states, at a low field, the relationship between SAR value and material properties of magnetic fluid is given by[11, 35]

$$SAR = \frac{P}{\rho\phi} = \frac{\mu_0 \chi_0 H_0^2}{2\rho\phi} \omega \frac{\omega\tau}{1+(\omega\tau)^2} \quad \text{..... (2)}$$

Where $P$ is the mean volumetric power dissipation, ρ the density of magnetic material, $\phi$ the volume fraction of nanoparticles in the suspension, $\mu_0$ the magnetic permeability, $H_0$ the magnetic field, ω the frequency of the applied ACMF, $\chi_0$ the susceptibility and τ the relaxation time. Both $\chi_0$ and τ have strong dependence on size, shape and inter-particle interactions. For a conservative estimation considering the lower bound of P, we can take $\chi_0$ as the chord susceptibility corresponding to the Langevin equation $L(\xi) = \coth \xi - 1/\xi$, where $\xi = \frac{\mu_0 M_S H V_m}{\phi k_B T}$, $M_S$ is the saturation magnetization.

In small AC field range $L(\xi) \approx \xi / 3$ and then the chord susceptibility is:

$$\chi_0 = \frac{\mu_0 V_m M_S^2}{3\phi k_B T} \quad \text{..... (4)}$$

The replacement of chord susceptibility in equation 3 gives us the direct relation between $M_S$ and the SAR, i.e. SAR is directly proportional to the magnetization values.

Another material related parameter which strongly influences the SAR value is the Neel-Brown relaxation time,[11, 36]

$$\tau = \frac{M_S}{2\gamma_0 K_{eff}^{3/2}} \left( \frac{\pi k_B T}{V} \right)^{1/2} \exp\left( \frac{K_{eff} V}{k_B T} \right) \text{..... (5)}$$

By introducing the relaxation time in the energy dissipation equation we can observe that τ is exponentially dependent on the product of $K_{eff}$ and $V$. From equation 3, 4 and 5, it is clear that the high $M_S$ values lead to a higher SAR value while high magneto-crystalline anisotropy ($K_{eff}$) leads to a shift in the critical particle size corresponding to maximum heating to a lower particle size value (since critical diameter corresponding to maximum heating $R_0$ α $1/K_{eff}$, ESI) whereas the lower particle moment suppresses the heating capability of nanomaterials.[11] In our case, the critical size corresponding to maximum heating is found to be 6, 15 and 27 nm for $CoFe_2O_4$, $Fe_3O_4$ and $MnFe_2O_4$ nanocrystals respectively. As the nanocrystal size of 25-60 nm $MFe_2O_4$ MNNAs is 4 ± 1 nm, higher SAR values are expected for $CoFe_2O_4$ MNNAs than the other ferrites. However, the 25-60 nm $CoFe_2O_4$ nanocrystals possess low $M_S$ value resulting in low observed values of SAR in comparison to similar sized $Fe_3O_4$ MNNAs. On other hand, for $MnFe_2O_4$ MNNAs, the low $K_{eff}$ and small nanocrystals size leads to even lesser SAR values. The intermediate $K_{eff}$ and $M_S$ values of $Fe_3O_4$ MNNAs make it the most suitable candidate to produce high heating power than Mn and Co ferrite.

We also investigated the heating performance of different nanocrystalline size (4-22 nm) $MFe_2O_4$ MNNAs (50-135 nm), which is depicted in Fig. 8c. The detailed analysis of SAR results as a function of nanocrystallite size of $MFe_2O_4$ MNNAs is shown in Fig. 8d. The variation of SAR in the MNNAs denotes a characteristic local maxima corresponding to the critical nanocrystals' diameter '$R_0$' for the Néel relaxation time at the corresponding frequency. For example, $MnFe_2O_4$ and $Fe_3O_4$ MNNAs show maxima at a nanocrystalline size of 14 nm, i.e. 80 nm size MNNAs while $CoFe_2O_4$ MNNAs shows the maximum heating efficiency for 4 nm size nanocrystals, i.e. 50 nm size MNNAs. It is of interest to note that by both (a) magnetic coupling

via control $MFe_2O_4$ MNNAs size from 25-60 nm with keeping nanocrystals size same and (b) controlling $MFe_2O_4$ MNNAs size 50-135 nm by controlling nanocrystals size, we are able to control the magnetic heating efficiency of the nanoassemblies. Further, to compare the heating performance of these MNNAs with their single domain counterparts, uniform ($\sigma < 15\%$) 4-22 nm size $Fe_3O_4$ nanoparticles are prepared using our previously published protocol (ESI).[34] As compared to the single domain counterparts, the SAR values recorded for $Fe_3O_4$ MNNAs are much higher (Fig. 9). This enhanced heating ability of MNNAs against their single domain counterparts, is attributed to the occurrence of strong magnetic coupling in MNNAs. This coupling is responsible for inducing a relatively more coherent magnetization reversal as well a relatively shorter spin relaxation under the applied ac field. Moreover, the additionally increased $K_{eff}$ due to strong magnetic coupling, also shifts the $R_0$ value to lower nanocrystal size.[37] It was thus observed that above 14 nm nanocrystals size, the SAR value decreases, since in larger size nanocrystals, losses are mainly due to Brownian relaxation.

Various researchers have attempted to utilize the heat generated by magnetic nanoparticles under ACMF in the direction of treatment of cancer at elevated temperatures (Magnetic hyperthermia).[38, 39] In order to evaluate the pharmacological application of magnetic hyperthermia, cytocompatibility study was carried out and subsequently the effect of magnetic nanoparticles on the population of HeLa cells in presence of ACMF was investigated. Sulphorhodamine-B (SRB) assay was carried out for determining the viable cell population in the dose-dependent cytocompatibility study of $MFe_2O_4$ MNNAs of particle size 80 nm. The dye binds to the basic amino acids of cellular proteins and the colorimetric evaluation of the same provides an estimate of total protein mass, which is directly proportional to the number of viable cells in the culture population. Fig. 10a shows the percentage viability of HeLa cells after 24 h

incubation of stable aqueous suspension of $MFe_2O_4$ MNNAs. The SRB assay showed that about above 90 % of the cells are viable, even after incubation with 1 mg/ml of $MFe_2O_4$ MNNAs. These results indicate that the viability and cell proliferation activity of HeLa cells is not affected by the presence of $MFe_2O_4$ MNNAs, suggesting that nanoassemblies are reasonably biocompatible and do not have toxic effects making them suitable for further *in vivo* use, which remains to be validated.

Fig. 10b represents the effect of ACMF on HeLa cell population in the presence of $Fe_3O_4$ MNNA. The cell suspension with MNNAs but without the ACMF (data not shown) and cell suspension without MNNAs but with application of ACMF serves as control. The control group hardly shows any reduction in the viable cell population. However, the cell population was reduced to 15% by the application of ACMF for a short period of 15 min. An increase in the time for which the cell suspension was exposed to the ACMF (treatment time) depicts an appreciable reduction in the cancer cell population, thereby establishing the potential of these nanoassemblies in hyperthermic treatment of cancer. The effect of hyperthermic treatment was also evaluated from the change in the cellular morphology under an optical microscope. The images reveal that the increase in the surrounding temperature initiates the degradation of cell membrane leading to cell death in the cancer cell line (Fig. 11). The increase in the treatment time is seen to initially disrupt the plasma membrane followed by degradation and perforation of cytoplasm observed for exposures times more than 20 min.

## 4. Conclusions

$MFe_2O_4$ (M = Mn, Fe, Co or Ni) nanoassemblies have been synthesized via thermal decomposition of metal chloride in glycol medium in the presence of ethylenediamine (EDA). Magnetic properties of these nanoassemblies are largely dependent on the volume, inter-particle

interaction and divalent cation electron configurations of each spinel ferrite. The collective Néel relaxation of nanocrystals within the assemblies and high magnetic moment of MNNAs enhances the heating ability to 2-4 times higher than the single domain counterpart. The moderate $K_{eff}$ and high $M_S$ values of $Fe_3O_4$ MNNAs make it most suitable candidate to produce high heating power than Mn and Co ferrite. These magnetic MNNAs are also efficient in reducing the cancer cell population by the application of ACMF even for short treatment times. Thus, the current work establishes these MNNAs as promising heating agents and opens the avenues of exploring magnetic hyperthermia as a potential therapeutic in addition or as an alternative to the classical chemotherapy.

**Acknowledgement:** We gratefully acknowledge the Industrial Research and Consultancy Center (IRCC), IIT Bombay, Council of Scientific and Industrial Research (CSIR), New Delhi, Nanomission of the Department of Science and Technology (DST) and nanotechnology division of DEIT, Government of India for the financial support of this work.

**References**

1. Y.-w. Jun, J.-w. Seo and J. Cheon, *Acc. Chem. Res.*, 2008, **41**, 179-189.
2. J.-H. Lee, Y.-M. Huh, Y.-w. Jun, J.-w. Seo, J.-t. Jang, H.-T. Song, S. Kim, E.-J. Cho, H.-G. Yoon and J.-S. Suh, *Nat. Med.*, 2006, **13**, 95-99.
3. K. Yan, P. Li, H. Zhu, Y. Zhou, J. Ding, J. Shen, Z. Li, Z. Xu and P. K. Chu, *RSC Adv.*, 2013, **3**, 10598-10618.
4. S. Chandra, K. C. Barick and D. Bahadur, *Adv. Drug Delivery Rev.*, 2011, **63**, 1267-1281.
5. S. Chandra, S. Nigam and D. Bahadur, *J. Biomed. Nanotechnol.*, 2014, **10**, 32-49.
6. S. A. Stanley, J. E. Gagner, S. Damanpour, M. Yoshida, J. S. Dordick and J. M. Friedman, *Science*, 2012, **336**, 604.
7. S. Rittikulsittichai, B. Singhana, W. W. Bryan, S. Sarangi, A. C. Jamison, A. Brazdeikis and T. R. Lee, *RSC Adv.*, 2013, **3**, 7838-7849.

8. L. Pradhan, R. Srivastava and D. Bahadur, *Acta Biomater.*, 2014, **10**, 2976-2987.
9. S. Kumar, A. Daverey, N. K. Sahu and D. Bahadur, *J. Mater. Chem. B*, 2013, **1**, 3652-3660.
10. D. Yoo, J.-H. Lee, T.-H. Shin and J. Cheon, *Acc. Chem. Res.*, 2011, **44**, 863-874.
11. R. E. Rosensweig, *J. Magn. Magn. Mater.*, 2002, **252**, 370-374.
12. X. L. Liu, H. M. Fan, J. B. Yi, Y. Yang, E. S. G. Choo, J. M. Xue, D. D. Fan and J. Ding, *J. Mater. Chem.*, 2012, **22**, 8235-8244.
13. D. Maity, P. Chandrasekharan, C.-T. Yang, K.-H. Chuang, B. Shuter, J.-M. Xue, J. Ding and S.-S. Feng, *Nanomedicine*, 2010, **5**, 1571-1584.
14. J.-H. Lee, J.-t. Jang, J.-s. Choi, S. H. Moon, S.-h. Noh, J.-w. Kim, J.-G. Kim, I.-S. Kim, K. I. Park and J. Cheon, *Nature Nanotech.*, 2011, **6**, 418-422.
15. P. Guardia, R. Di Corato, L. Lartigue, C. Wilhelm, A. Espinosa, M. Garcia-Hernandez, F. Gazeau, L. Manna and T. Pellegrino, *ACS Nano*, 2012, **6**, 3080-3091.
16. P. Hugounenq, M. Levy, D. Alloyeau, L. Lartigue, E. Dubois, V. Cabuil, C. Ricolleau, S. Roux, C. Wilhelm, F. Gazeau and R. Bazzi, *J. Phys. Chem. C*, 2012, **116**, 15702-15712.
17. L. Lartigue, P. Hugounenq, D. Alloyeau, S. P. Clarke, M. Lévy, J.-C. Bacri, R. Bazzi, D. F. Brougham, C. Wilhelm and F. Gazeau, *ACS Nano*, 2012, **6**, 10935-10949.
18. K. C. Barick, M. Aslam, Y.-P. Lin, D. Bahadur, P. V. Prasad and V. P. Dravid, *J. Mater. Chem.*, 2009, **19**, 7023-7029.
19. W. Strober, in *Curr. Protoc. Immunol.*, John Wiley & Sons, Inc., 2001.
20. S. Chandra, S. Mehta, S. Nigam and D. Bahadur, *New J. Chem.*, 2010, **34**, 648-655.
21. Z. Xu, C. Shen, Y. Hou, H. Gao and S. Sun, *Chem. Mater.*, 2009, **21**, 1778-1780.
22. M. Aslam, E. A. Schultz, T. Sun, T. Meade and V. P. Dravid, *Crystal Growth & Design*, 2007, **7**, 471-475.
23. S. Xuan, Y.-X. J. Wang, J. C. Yu and K. Cham-Fai Leung, *Chem. Mater.*, 2009, **21**, 5079-5087.
24. Z. Huang and F. Tang, *J. Colloid Interface Sci.*, 2005, **281**, 432-436.
25. L. Gou and C. J. Murphy, *J. Mater. Chem.*, 2004, **14**, 735-738.
26. C. Cheng, F. Xu and H. Gu, *New J. Chem.*, 2011, **35**, 1072-1079.
27. A. Mitra, J. Mohapatra, S. S. Meena, C. V. Tomy and M. Aslam, *J. Phys. Chem. C*, 2014, **118**, 19356-19362.

28. K. Nadeem, H. Krenn, T. Traussnig, R. Wurschum, D. Szabo and I. Letofsky-Papst, *J. Appl. Phys.*, 2012, **111**, 113911-113911-113916.
29. J. Mohapatra, A. Mitra, D. Bahadur and M. Aslam, *J. Alloys Compd.*, 2015, **628**, 416-423.
30. Q. Song and Z. J. Zhang, *J. Phys. Chem. B*, 2006, **110**, 11205-11209.
31. S. Qin, L. Wang, X. Zhang and G. Su, *Appl. Surf. Sci.*, 2010, **257**, 731-735.
32. L. G. Bach, M. R. Islam, J. T. Kim, S. Seo and K. T. Lim, *Appl. Surf. Sci.*, 2012, **258**, 2959-2966.
33. A. Kostopoulou, K. Brintakis, M. Vasilakaki, K. N. Trohidou, A. P. Douvalis, A. Lascialfari, L. Manna and A. Lappas, *Nanoscale*, 2014, **6**, 3764-3776.
34. J. Mohapatra, A. Mitra, D. Bahadur and M. Aslam, *CrystEngComm*, 2013, **15**, 524-532.
35. J. Carrey, B. Mehdaoui and M. Respaud, *J. Appl. Phys.*, 2011, **109**, 083921-083917.
36. E. L. Verde, G. T. Landi, J. A. Gomes, M. H. Sousa and A. F. Bakuzis, *J. Appl. Phys.*, 2012, **111**, 123902.
37. M. Jeun, S. Bae, A. Tomitaka, Y. Takemura, K. H. Park, S. H. Paek and K.-W. Chung, *Appl. Phys. Lett.*, 2009, **95**, 082501.
38. K. Hayashi, K. Ono, H. Suzuki, M. Sawada, M. Moriya, W. Sakamoto and T. Yogo, *ACS Appl. Mater. Interfaces*, 2010, **2**, 1903-1911.
39. K. C. Barick, S. Singh, N. V. Jadhav, D. Bahadur, B. N. Pandey and P. A. Hassan, *Adv. Funct. Mater.*, 2012, **22**, 4975-4984.

## Figures

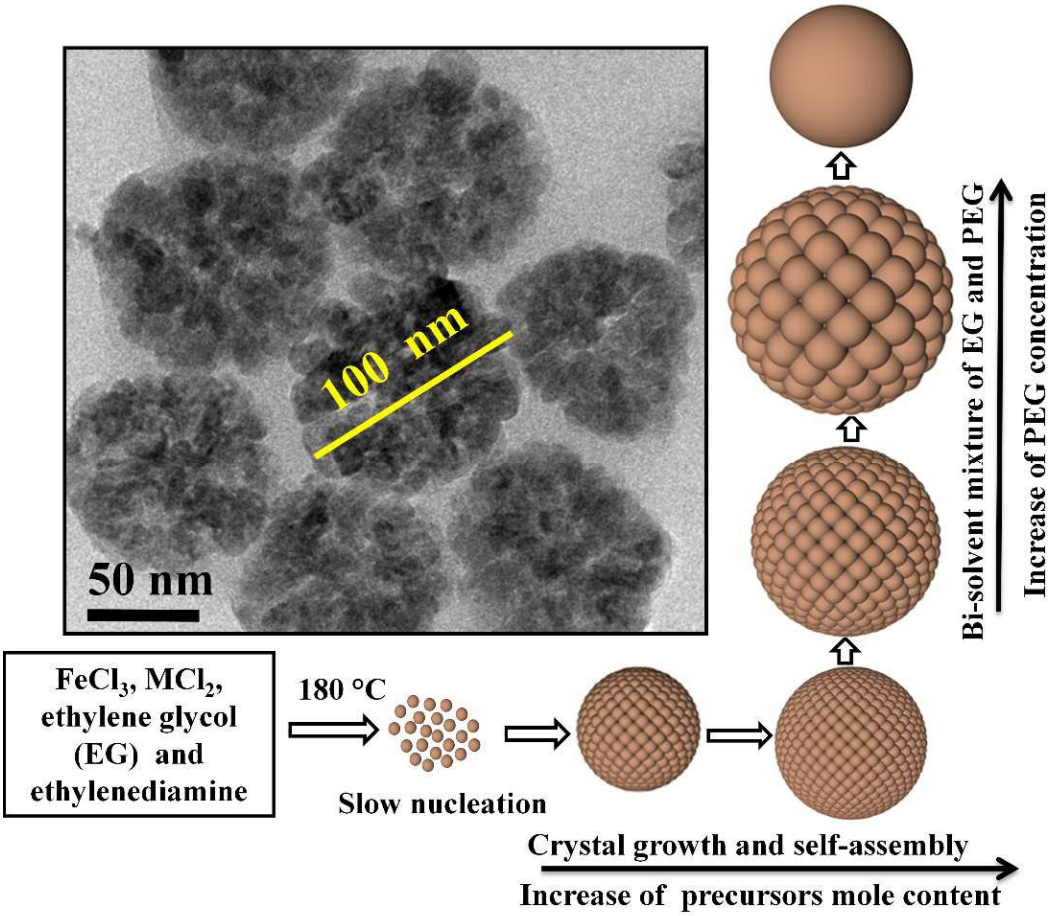


**Scheme1**. Schematic representation for the synthesis of monodisperse $MFe_2O_4$ nanocrystals nanoassembly with tunable grain size and particle size. With maintaining the nanocrystalline size same, the nanoassemblies size is controlled in the range of 25-60 nm by variation of Fe-precursor mole content to ethylene glycol (EG). The use of a bi-solvent mixture of ethylene glycol and polyethylene glycol (PEG-400) leads control of nanoassemblies size from 60 to 135 nm.

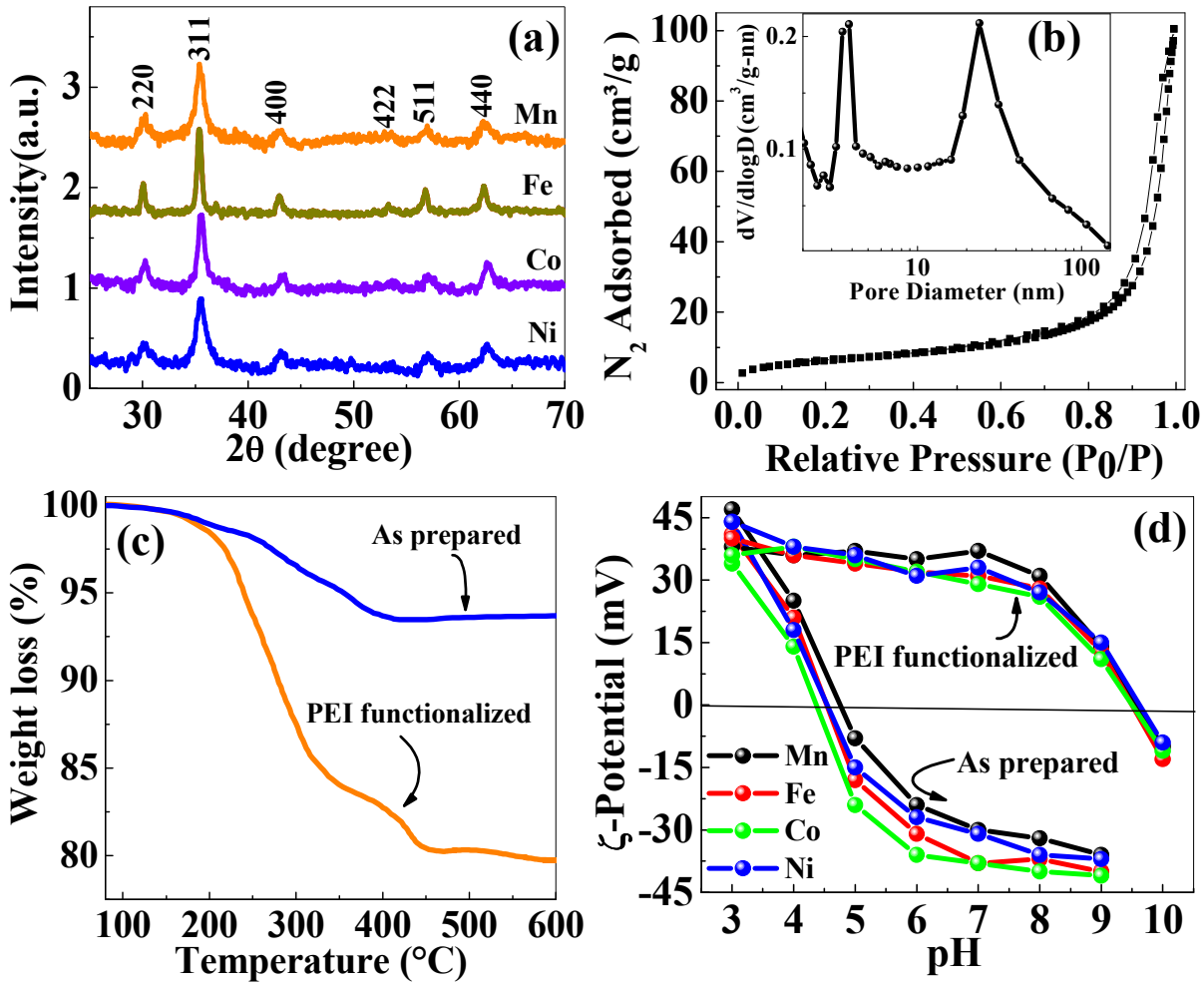


**Fig. 1** (a) XRD patterns of $MFe_2O_4$ MNNAs (80 nm) produced with 5 ml of PEG. (b) Surface area and porosity of $Fe_3O_4$ MNNAs (80 nm) determined by $N_2$ adsorption and desorption isotherms. Inset shows the pore size distribution, the first peak at 4 nm corresponding to the pore diameter of the nanoassembly and the other peak at 30 nm assigned to the inter-space among the nanoassembly. (c) Thermogravimetric plot of as prepared and PEI functionalized $Fe_3O_4$ MNNAs (80 nm). (d) Zeta potential at different pH values of as prepared and PEI functionalized $Fe_3O_4$ MNNAs (80 nm).

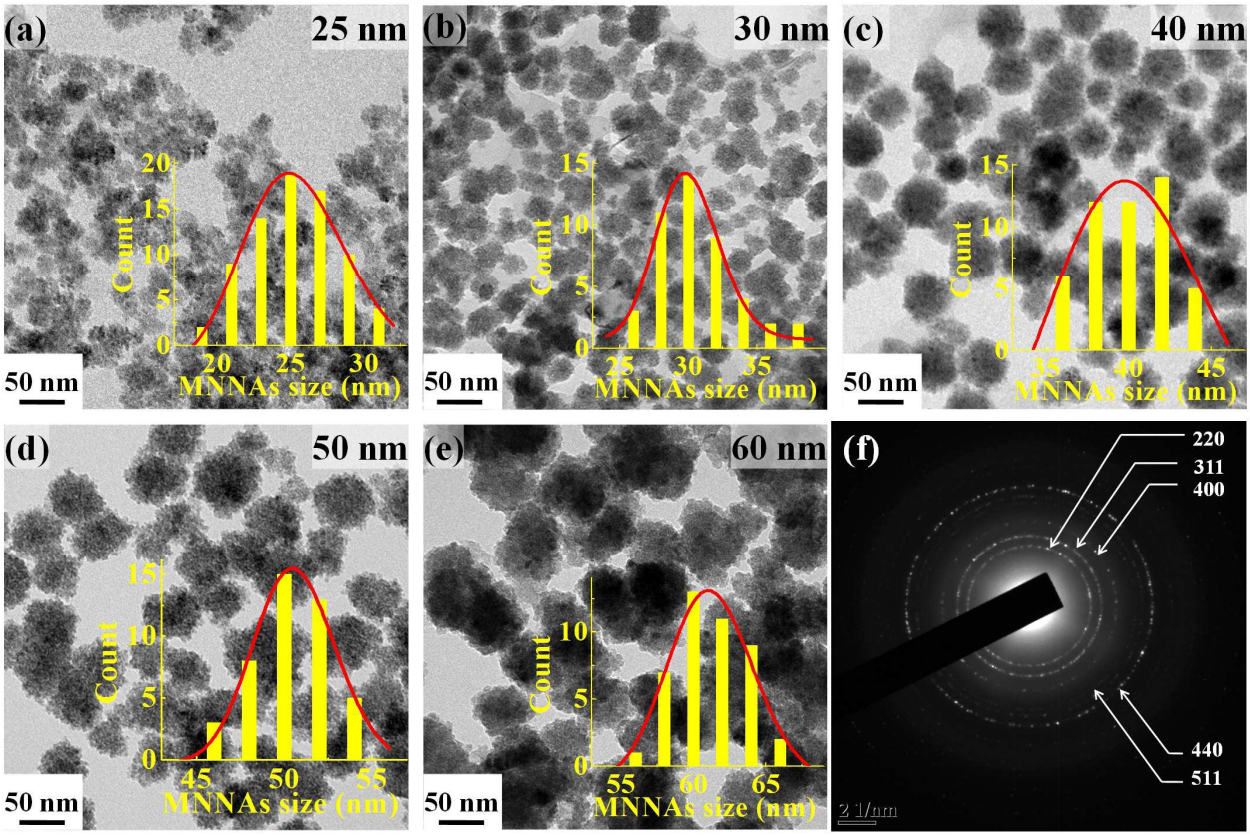


**Fig. 2** TEM images of the $Fe_3O_4$ MNNAs, obtained using different mole content of Fe-precursor ($Fe^{3+}/Fe^{2+}$ = 2:1): (a) 1.5 mmol (25 nm), (b) 3 mmol (30 nm), (c) 4.5 mmol (40 nm), (d) 6 mmol (50 nm), and (e) 7.5 mmol (60 nm). (f) Selected area electron diffraction (SAED) pattern of $Fe_3O_4$ nanoparticles. Inset of the individual TEM image demonstrates the histogram of the particle size distribution. All the samples show uniform distribution with a standard deviation σ ≤ 20 %.

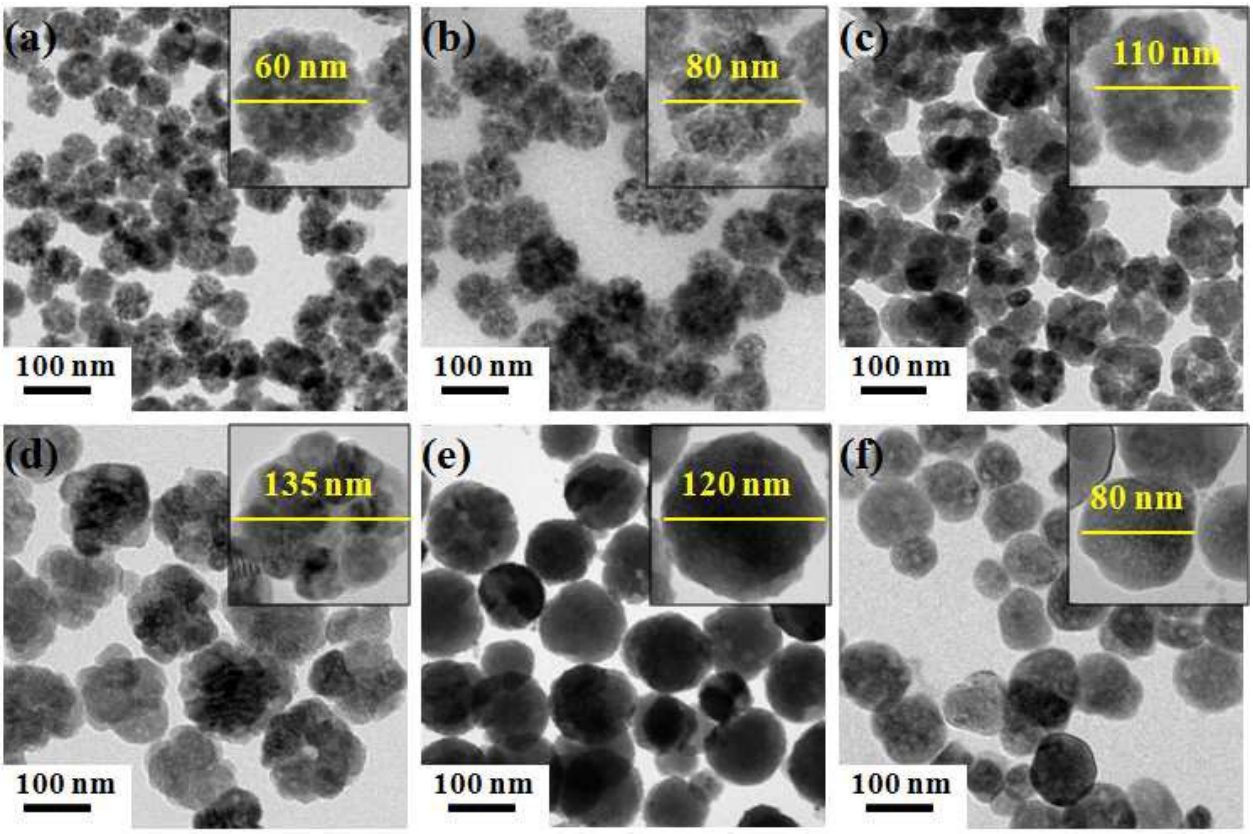


**Fig. 3** TEM images of $Fe_3O_4$ prepared with different amount of PEG; (a) 2 ml (60 nm), (b) 5 ml (80 nm), (c) 8 ml (110 nm), (d) 12 ml (135 nm), (e) 16 ml (120 nm) and (f) 20 ml (80 nm). Inset shows their respective HRTEM image. The histograms of the particle size distribution of 60-135 nm sized $Fe_3O_4$ MNNAs is shown in Fig. S4. All the $Fe_3O_4$ MNNAs prepared using PEG 2-12 ml show uniform distribution with a standard deviation $\sigma \leq 20$ %.

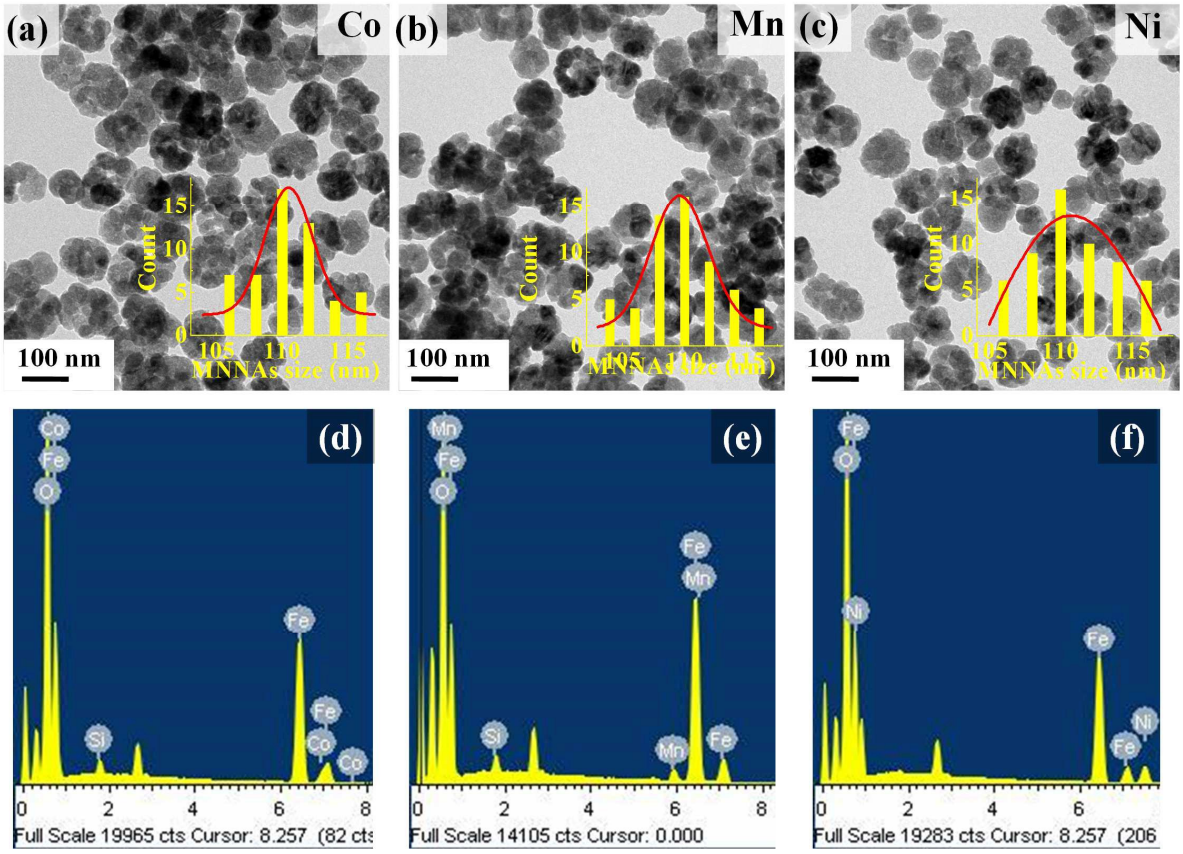


**Fig. 4:** TEM micrographs of 110 nm sized $MFe_2O_4$ MNNAs prepared by using 8 ml of PEG: (a) $MnFe_2O_4$, (b) $CoFe_2O_4$ and (c) $NiFe_2O_4$. Inset of the individual TEM image demonstrates the histogram of the MNNAs size distribution. The corresponding energy dispersion X-ray spectrum (EDS): (d) $MnFe_2O_4$, (e) $CoFe_2O_4$ and (f) $NiFe_2O_4$.

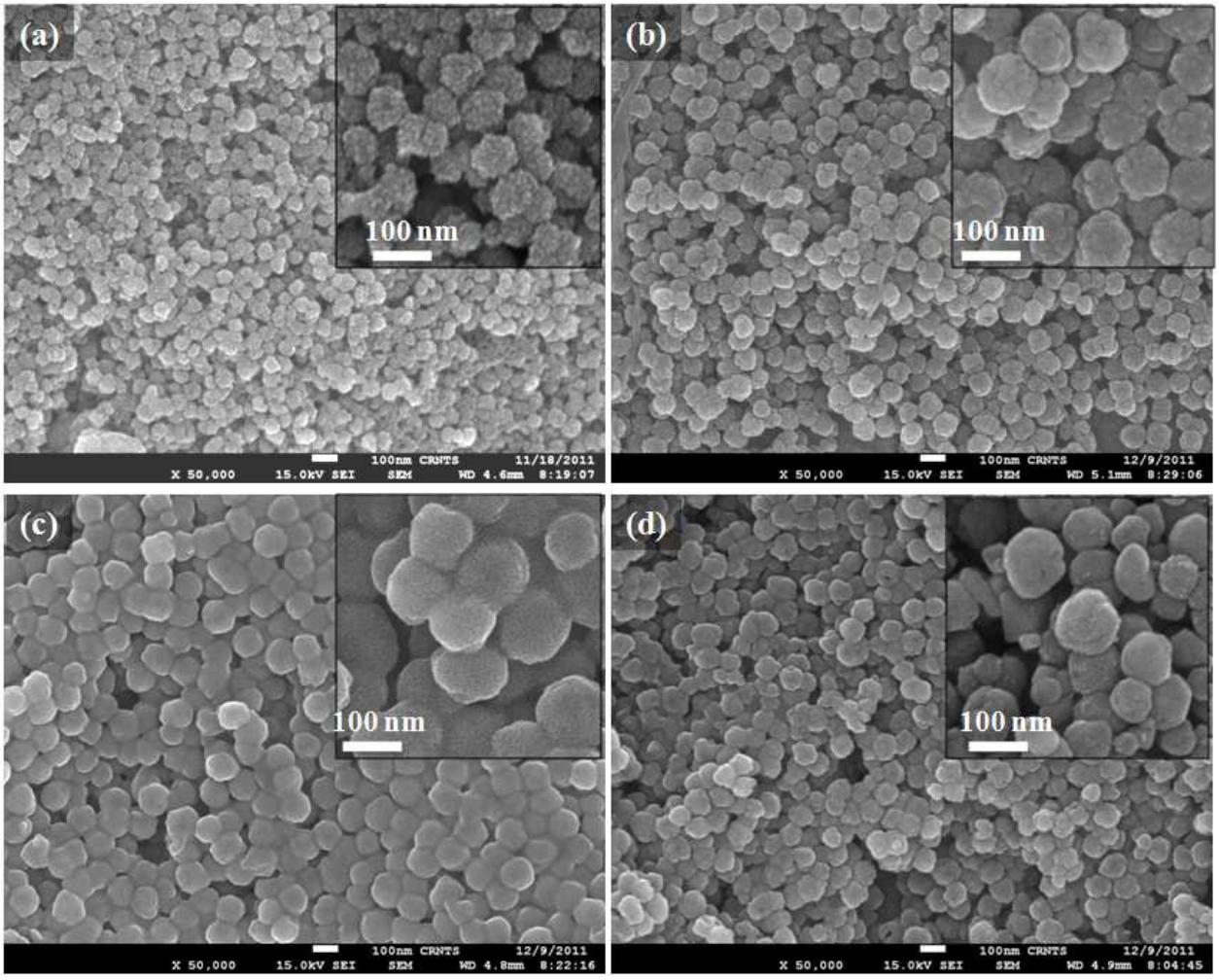


**Fig. 5** FEG-SEM images of the $Fe_3O_4$ MNNAs obtained using different amount of PEG content: (a) 2 ml (60 nm), (b) 5 ml (80 nm), (c) 16 ml (120 nm) and (d) 20 ml (80 nm). Inset shows the corresponding high resolution SEM image.

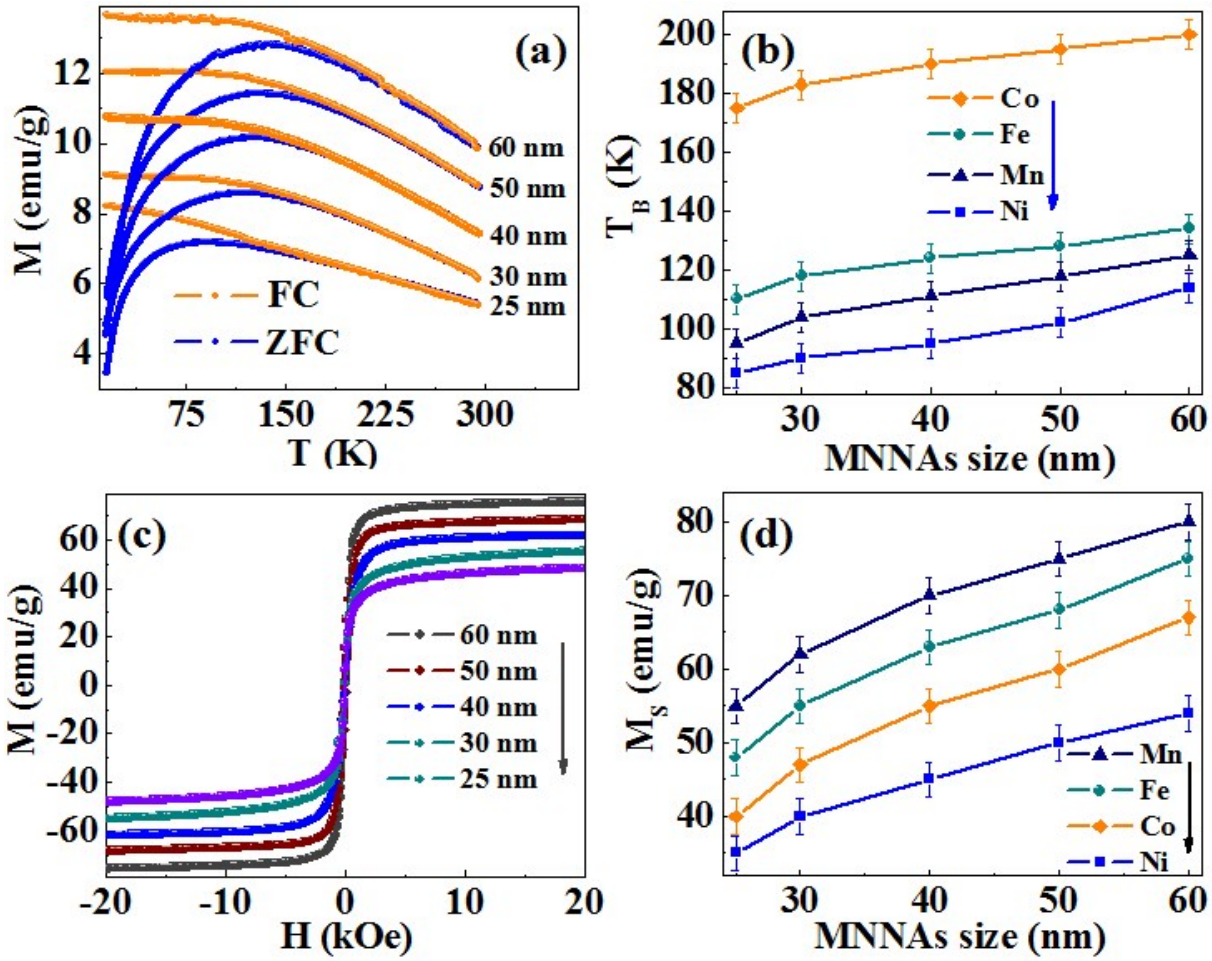


**Fig. 6** (a) Temperature dependence of low field (200 Oe) ZFC-FC magnetization of different size $Fe_3O_4$ MNNAs ($\sigma \leq 20$ %). prepared using EG as solvent. (b) Blocking temperature vs. MNNA size plot of all $MFe_2O_4$ MNNAs ($\sigma \leq 20$ %), where M is Mn, Fe, Co and Ni. (c) Superimposed hysteresis curves of different size $Fe_3O_4$ MNNAs prepared using EG as solvent. (d) $M_S$ value vs. MNNA size plot of all $MFe_2O_4$ MNNAs.

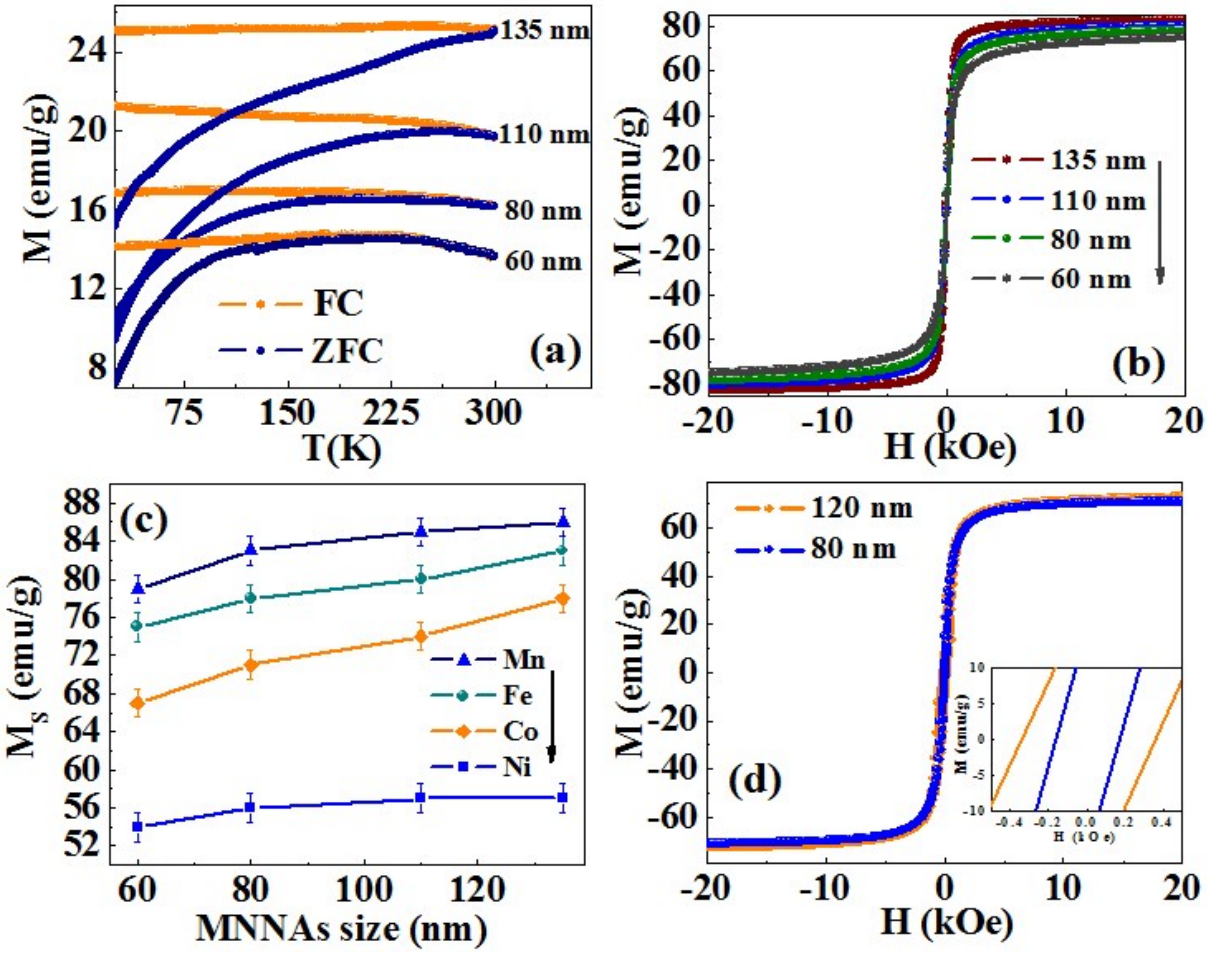


**Fig. 7** (a) Temperature dependence of low field (200 Oe) ZFC-FC magnetization plot and (b) room temperature field dependent magnetization loop of $Fe_3O_4$ MNNAs of different size produced by varying PEG content from 0 to 12 ml. (c)The variation of room temperature $M_S$ with particle size for all $MFe_2O_4$ MNNAs ($\sigma \leq 20$ %). (d) Superimposed hysteresis curves of 100 and 80 nm $Fe_3O_4$ nanoparticles produced at with higher content of PEG.

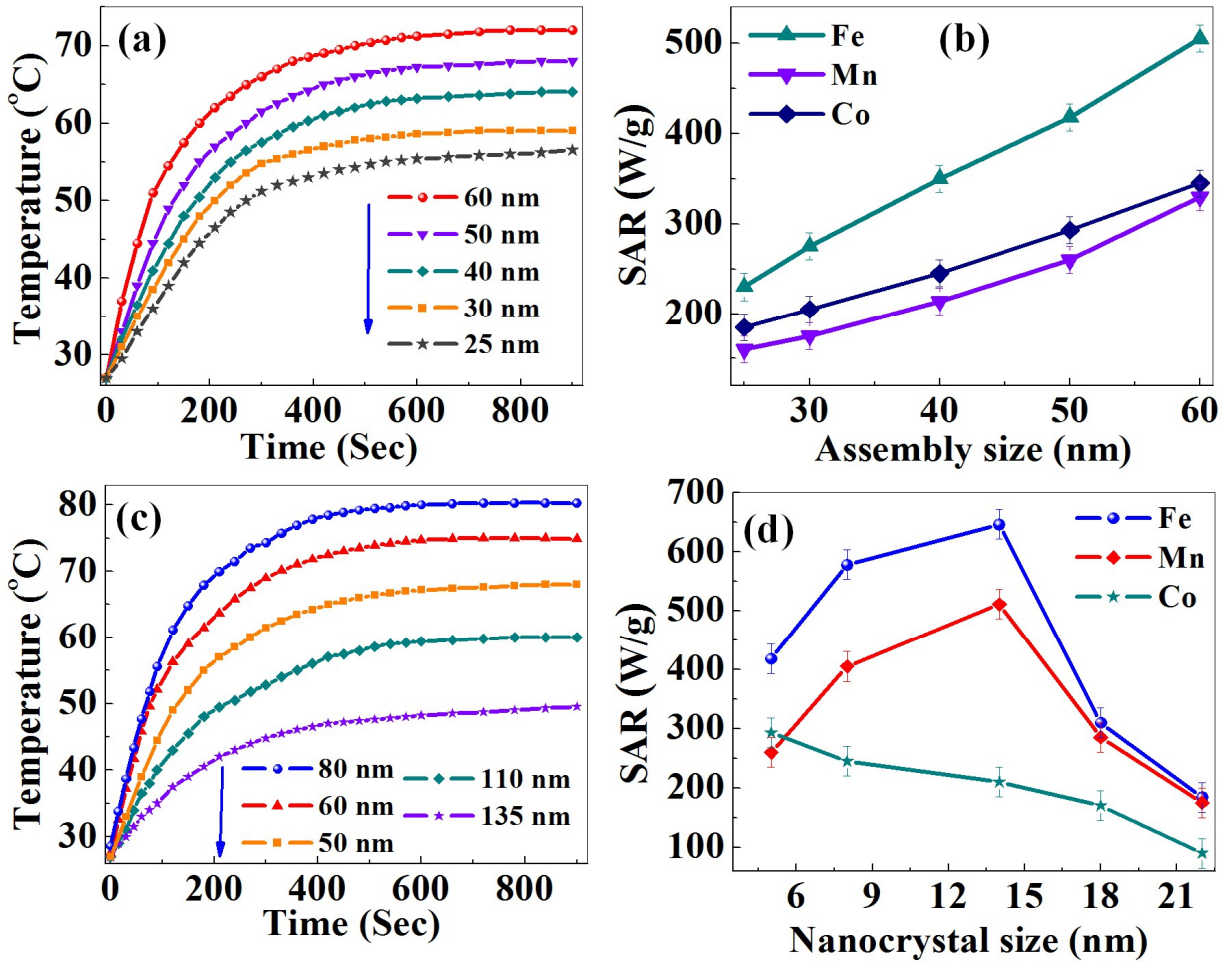


**Fig. 8** (a) Time dependent calorimetric profiles for aqueous suspension (2 mg/ml) of $Fe_3O_4$ MNNAs (25-60 nm; same nanocrystal size) under an AC magnetic field (310 Oe) and (b) the corresponding specific absorption rate (SAR) as a function of nanoassembly size of MNNAs. (c) Time dependent calorimetric profiles for aqueous suspension (2 mg/ml) of $Fe_3O_4$ MNNAs (50-135 nm; varying nanocrystal size) under an AC magnetic field (310 Oe) and (d) the corresponding specific absorption rate (SAR) as a function of nanoassembly size of MNNAs. A complete demonstration of the optimization of heat activation efficiency of $MFe_2O_4$ nanocrystals nanoassemblies (MNNAs) by controlling size, composition and magnetic coupling among the nanocrystals within the MNNAs are shown in Fig. S7 (ESI).

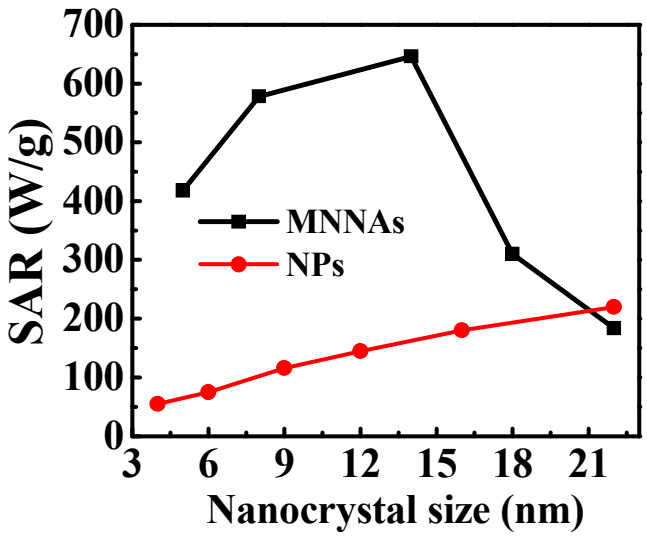


**Fig. 9** Specific absorption rate (SAR) as a function of nanocrystallite size of $Fe_3O_4$ MNNAs and NPs. This higher SAR value of MNNAs against their single domain counterparts is due to presence of strong magnetic coupling between nanocrystals with in the MNNAs. This coupling enhances saturation magnetization and leads a relatively more coherent magnetization reversal under the applied ac field and thus results the higher SAR for MNNAs than nanoparticles.

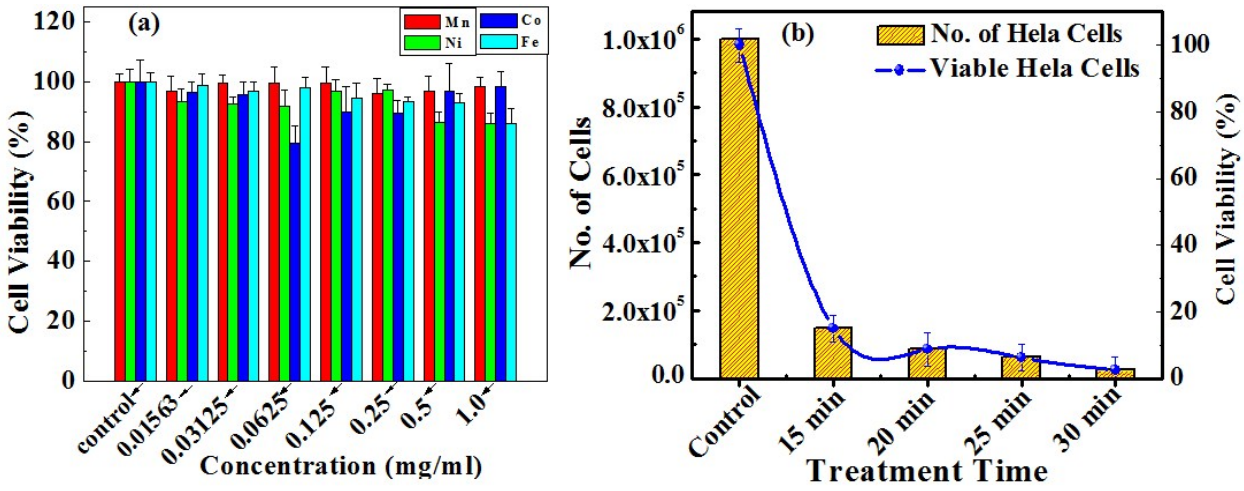


**Fig. 10** Percentage viability of HeLa cells after 24 h incubation of stable aqueous suspension of amine functionalized $MFe_2O_4$ MNNAs (80 nm). The results are shown as mean ± standard deviation (n = 3). (b) Effect of ACMF on HeLa cell population in the presence of $Fe_3O_4$ MNNA.

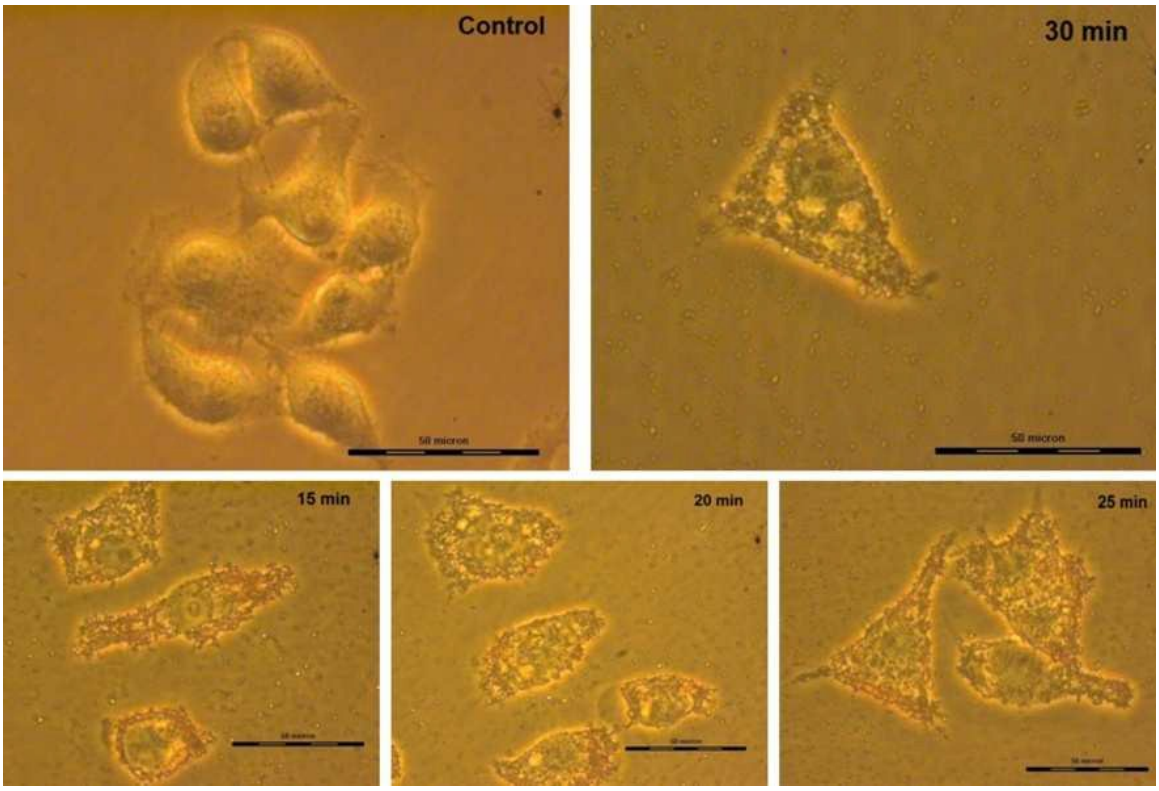


**Fig. 11** Images from optical microscope revealing the degradation of cell membrane and cytoplasm with various treatment times (the scale bar is 50 μm).

**Table 1:** Variation of nanocrystallite and MNNAs size with control of precursor to EG/PEG content.

| Metal precursor ($Fe^{3+}/M^{2+}$ = 2:1) (mM) | EG (ml) | PEG (ml) | Nanoassembly size (σ < 20 %) | Nanocrystallite size (d ± 1 nm) |
|---|---|---|---|---|
| 1.5 | 30 | Absence of PEG | 25 nm | 4 nm |
| 3 | 30 | | 30 nm | 4.6 nm |
| 4.5 | 30 | | 40 nm | 4.6 nm |
| 6 | 30 | | 50 nm | 4.8 nm |
| 7.5 | 30 | | 60 nm | 5 nm |
| 9 | 30 | | Non-uniform morphology | |
| 6 | 28 | 2 | 60 nm | 8 nm |
| 6 | 25 | 5 | 80 nm | 14 nm |
| 6 | 22 | 8 | 110 nm | 18 nm |
| 6 | 18 | 12 | 135 nm | 22 nm |

## Graphical Abstract